The Astrophysical Journal Letters, 951:L29 (12pp), 2023 July 10 https://doi.org/10.3847/2041-8213/acd93d

TOI-1859b: A 64 Day Warm Jupiter on an Eccentric and Misaligned Orbit

Jiayin Dong[1,2,3,32], Songhu Wang[4], Malena Rice[5,6,33], George Zhou[7], Chelsea X. Huang[7], Rebekah I. Dawson[2,3], Gudmundur K. Stefánsson[8,34], Samuel Halverson[9], Shubham Kanodia[10,35], Suvrath Mahadevan[2,3,11,36], Michael W. McElwain[12], Jaime A. Alvarado-Montes[13,14], Joe P. Ninan[2,3], Paul Robertson[15,37], Arpita Roy[16,17], Christian Schwab[13,14], Sarah E. Logsdon[18], Ryan C. Terrien[19], Karen A. Collins[20], Gregor Srdoc[21], Ramotholo Sefako[22], Didier Laloum[23], David W. Latham[20], Allyson Bieryla[20], Paul A. Dalba[24,25,33], Diana Dragomir[26], Steven Villanueva, Jr.[27,38], Steve B. Howell[28], George R. Ricker[5], S. Seager[5,29,30], Joshua N. Winn[8], Jon M. Jenkins[28], Avi Shporer[5], and David Rapetti[28,31]

[1] Center for Computational Astrophysics, Flatiron Institute, 162 Fifth Avenue, New York, NY 10010, USA; jdong@flatironinstitute.org
[2] Department of Astronomy & Astrophysics, 525 Davey Laboratory, The Pennsylvania State University, University Park, PA 16802, USA
[3] Center for Exoplanets and Habitable Worlds, 525 Davey Laboratory, The Pennsylvania State University, University Park, PA 16802, USA
[4] Department of Astronomy, Indiana University, Bloomington, IN 47405, USA
[5] Department of Physics and Kavli Institute for Astrophysics and Space Research, Massachusetts Institute of Technology, Cambridge, MA 02139, USA
[6] Department of Astronomy, Yale University, New Haven, CT 06511, USA
[7] University of Southern Queensland, Centre for Astrophysics, West Street, Toowoomba, QLD 4350, Australia
[8] Department of Astrophysical Sciences, Princeton University, 4 Ivy Lane, Princeton, NJ 08540, USA
[9] Jet Propulsion Laboratory, California Institute of Technology, 4800 Oak Grove Drive, Pasadena, CA 91109, USA
[10] Earth and Planets Laboratory, Carnegie Institution for Science, 5241 Broad Branch Road, NW, Washington, DC 20015, USA
[11] ETH Zurich, Institute for Particle Physics & Astrophysics, Zurich, Switzerland
[12] Exoplanets and Stellar Astrophysics Laboratory, NASA Goddard Space Flight Center, Greenbelt, MD 20771, USA
[13] School of Mathematical and Physical Sciences, Macquarie University, Balaclava Road, North Ryde, NSW 2109, Australia
[14] Research Centre for Astronomy, Astrophysics and Astrophotonics, Macquarie University, Balaclava Road, North Ryde, NSW 2109, Australia
[15] Department of Physics & Astronomy, The University of California, Irvine, Irvine, CA 92697, USA
[16] Space Telescope Science Institute, 3700 San Martin Drive, Baltimore, MD 21218, USA
[17] Department of Physics and Astronomy, Johns Hopkins University, 3400 N Charles Street, Baltimore, MD 21218, USA
[18] NSF's National Optical-Infrared Astronomy Research Laboratory, 950 N. Cherry Avenue, Tucson, AZ 85719, USA
[19] Carleton College, One North College Street, Northfield, MN 55057, USA
[20] Center for Astrophysics | Harvard & Smithsonian, 60 Garden Street, Cambridge, MA 02138, USA
[21] Kotizarovci Observatory, Sarsoni 90, 51216 Viskovo, Croatia
[22] South African Astronomical Observatory, P.O. Box 9, Observatory, Cape Town 7935, South Africa
[23] AAVSO, 185 Alewife Brook Parkway, Suite 410, Cambridge, MA 02138, USA
[24] Department of Astronomy and Astrophysics, University of California, Santa Cruz, CA 95064, USA
[25] SETI Institute, Carl Sagan Center, 339 Bernardo Avenue, Suite 200, Mountain View, CA 94043, USA
[26] Department of Physics and Astronomy, University of New Mexico, Albuquerque, NM, USA
[27] NASA Goddard Space Flight Center, Exoplanets and Stellar Astrophysics Laboratory (Code 667), Greenbelt, MD 20771, USA
[28] NASA Ames Research Center, Moffett Field, CA 94035, USA
[29] Department of Earth, Atmospheric, and Planetary Sciences, Massachusetts Institute of Technology, Cambridge, MA 02139, USA
[30] Department of Aeronautics and Astronautics, Massachusetts Institute of Technology, Cambridge, MA 02139, USA
[31] Research Institute for Advanced Computer Science, Universities Space Research Association, Washington, DC 20024, USA
Received 2023 April 2; revised 2023 May 17; accepted 2023 May 25; published 2023 July 7

Abstract

Warm Jupiters are close-in giant planets with relatively large planet–star separations (i.e., $10 < a/R_\star < 100$). Given their weak tidal interactions with their host stars, measurements of stellar obliquity may be used to probe the initial obliquity distribution and dynamical history for close-in gas giants. Using spectroscopic observations, we confirm the planetary nature of TOI-1859b and determine the stellar obliquity of TOI-1859 to be $\lambda = 38.9^{+2.8}_{-2.7}{}^\circ$ relative to its planetary companion using the Rossiter–McLaughlin effect. TOI-1859b is a 64 day warm Jupiter orbiting around a late F dwarf and has an orbital eccentricity of $0.57^{+0.12}_{-0.16}$ inferred purely from transit light curves. The eccentric and misaligned orbit of TOI-1859b is likely an outcome of dynamical interactions, such as planet–planet scattering and planet–disk resonance crossing.

Unified Astronomy Thesaurus concepts: Extrasolar gaseous giant planets (509); Exoplanet dynamics (490); Radial velocity (1332); Transit photometry (1709)

1. Introduction

Warm Jupiters are giant planets with planet–star separations $a/R_\star$ of ~10–100. Because of their wide orbital separations, warm Jupiters are expected to have weak tidal interactions with their host stars, such that they offer new insights into the origin channels of close-in giant planets. Tidal dissipation in the planet or in the star is not expected to be efficient enough to significantly modify a warm Jupiter's orbital eccentricity (unless its eccentricity is extremely high, such that $a(1-e^2)$ is small) and its host star's obliquity (see the review by

[32] Flatiron Research Fellow.
[33] 51 Pegasi b Fellow.
[34] NASA Hubble Fellow.
[35] Carnegie EPL Fellow.
[36] NEID Principal Investigator.
[37] NEID Instrument Team Project Scientist.
[38] NPP Fellow.

Ogilvie 2014 and references therein). Benefiting from this property, a warm Jupiter's dynamical features may be used as a probe of its original formation environment and dynamical history.

The eccentricities of known warm Jupiters are broadly distributed from circular to super eccentric orbits (with an eccentricity of 0.8 or higher), and the distribution could be bimodal (Dong et al. 2021). It is yet unclear which dynamical mechanisms predominantly sculpt the eccentricity distribution of warm Jupiters. One or more mechanisms, such as planet–planet scattering (Chatterjee et al. 2008; Nagasawa et al. 2008; Nagasawa & Ida 2011; Beaugé & Nesvorný 2012), stellar/planetary Kozai (see von Zeipel–Lidov–Kozai oscillations in von Zeipel 1910; Kozai 1962; Lidov 1962; and applications in Wu & Murray 2003; Fabrycky & Tremaine 2007; Naoz 2016; Vick et al. 2019), and other secular interactions (Wu & Lithwick 2011; Petrovich 2015) could be responsible for the high-e population. Either smooth disk migration or in situ formation origins (Duffell & Chiang 2015) could feasibly produce the low-e component of the distribution of warm Jupiters.

Notably, although these mechanisms can all broadly explain the bulk of observed eccentricities of warm Jupiters, they would generate different stellar obliquities, reflected through observations as different sky-projected spin–orbit angles of warm Jupiter systems. Secular chaos tends to produce mutual inclinations less than 90° (Teyssandier et al. 2019); stellar Kozai predicts bimodal mutual inclinations concentrated at 40° and 140° (Fabrycky & Tremaine 2007; Anderson et al. 2016; Vick et al. 2019); and planet–planet scattering with no Kozai effect predicts mutual inclinations spread from 0° to 60° (Chatterjee et al. 2008). Interpreting warm Jupiters' stellar obliquities with eccentricities is therefore a possible way to distinguish between different proposed mechanisms.

Measuring the stellar obliquity of warm Jupiter systems via the Rossiter–McLaughlin effect (RM effect; McLaughlin 1924; Rossiter 1924) is challenging because of the rarity of transit opportunities due to warm Jupiters' long orbital periods. As presented in the review article by Albrecht et al. (2022), only 25 warm/cold Jupiters have stellar obliquity measurements, compared to 105 hot Jupiters. Fortunately, the Transiting Exoplanet Survey Satellite (TESS; Ricker et al. 2015) is discovering a large sample of transiting warm Jupiters around bright stars that are suitable for the RM-effect follow-up observations (e.g., Dong et al. 2021).

In this work, we confirm the planetary nature of TOI-1859b, a 64 day warm Jupiter on an eccentric orbit, and measure the stellar obliquity using the NEID spectrograph. This measurement is the sixth result from the Stellar Obliquities in Long-period Exoplanet Systems survey (Rice et al. 2021, 2022b, 2023; Wang et al. 2022), which was designed to expand the set of spin–orbit constraints for exoplanets on wide orbits. Stellar obliquity constraints for systems spanning a wide range of orbital eccentricities are particularly important to inform whether trends with properties such as host star temperatures (Schlaufman 2010; Winn et al. 2010; Albrecht et al. 2012; Wang et al. 2021) and planet mass hold as a function of eccentricity (e.g., Rice et al. 2022a).

In Section 2, we describe the detection of the TESS transit signal and validation of the signal from ground-based follow-up observations. In Section 3, we present the modeling of stellar properties and planetary properties, and lastly, in Section 4, we summarize our discovery and discuss the interpretation of warm Jupiters' stellar obliquities.

2. Observations

2.1. TESS Photometry

As a continuous-viewing-zone target, TOI-1859 has been observed in more than 20 TESS sectors over the span of 4 yr. The TESS Cycle 2 observations from Sectors 14–20 and 22–26 (UT 2019 July 18 to UT 2020 July 4) lead to the initial detection of planetary transit signals. Subsequent Cycle 4 observations in TESS Sectors 40, 41, 47–50, and 52–55 refine the ephemeris and transit timings. In the ongoing TESS Cycle 5, TOI-1859 has been observed for four more sectors from Sectors 56, 57, 59, and 60. The TESS data products include postage stamps at 2 minute time sampling and full-frame images with 30 minute sampling. Notably, starting from Sector 56, the 20 s cadence postage stamps of TOI-1859 are available, enabling future asteroseismology studies.

The transit signal of TOI-1859b was detected independently by the NASA Science Processing Operations Center (SPOC) pipeline (Jenkins et al. 2016) and the MIT Quick-Look Pipeline (Huang et al. 2020a, 2020b). A single transit of TOI-1859b was detected in the SPOC transit search (Jenkins 2002; Jenkins et al. 2010, 2020) in Sector 15. The true period was identified in a search of Sector 14–23 in which the signature was fitted with a limb-darkened transit model (Li et al. 2019) and passed all the data validation diagnostic tests (Twicken et al. 2018). A recent search of Sector 14–60 located the source of the transits to within $0\farcs473 \pm 2\farcs6$. We use the 2 minute cadence SPOC PDC_SAP light curves (Smith et al. 2012; Stumpe et al. 2012, 2014), for which the image data were reduced and analyzed by the SPOC at NASA Ames Research Center, for the analysis in this work. The TESS data are presented in Figure 1. We found the overall bias on the determination of the planet radius due to bias in the sky background correction in the TESS primary mission (which comprises Sectors 14–26 data) is much smaller than the uncertainty on transit depth and therefore negligible.

2.2. Ground-based Transit Photometry

Two additional transits of TOI-1859b were obtained from ground-based facilities led by the TESS Follow-up Observing Program seeing-limited photometry group (Collins 2019). We used the `TESS Transit Finder`, which is a customized version of the `Tapir` software package (Jensen 2013), to schedule our transit observations. Differential photometric data were extracted using `AstroImageJ` (Collins et al. 2017). These observations cleared the field for nearby eclipsing binaries and verified that the transit events detected by TESS were on target relative to known Gaia DR3 stars. The transit observations are presented in Figure 1.

1. We observed a full transit window on UT 2021 March 23 in *Ic* band from the 0.2 m telescope at the Private Observatory of the Mount (OPM) near Saint-Pierre-du-Mont, France. The telescope is equipped with a 3326×2504 pixel Atik 383 L+ camera having an image scale of $0\farcs69$ per pixel, resulting in a $38' \times 29'$ field of view. A transit-like event with a depth of ~5000 ppm was detected using a circular photometric aperture with radius

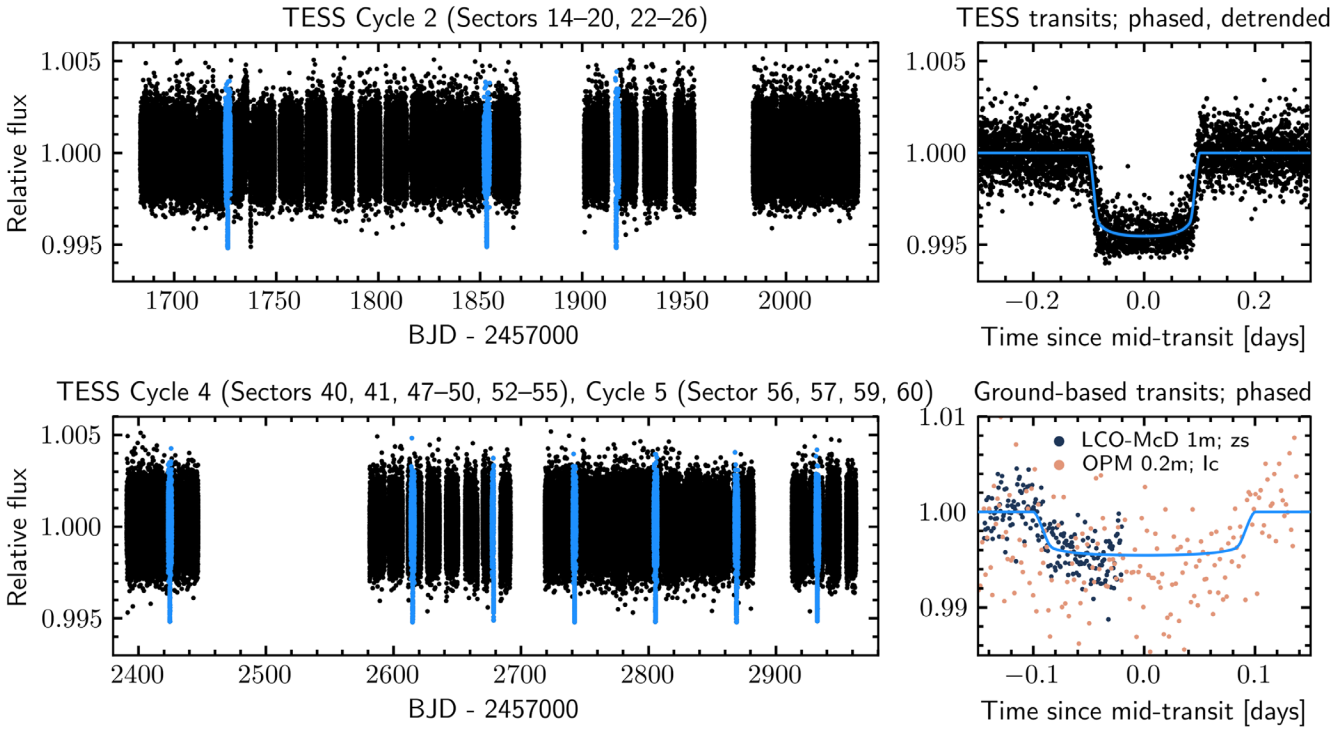

Figure 1. TESS SPOC PDC_SAP light curves and ground-based transits of TOI-1859b. TOI-1859b transits are labeled in blue on TESS light curves in the left two panels. The median of the fitted transit model is plotted in blue on the two right panels. Two ground-based transits are shown in the lower right panel.

8.″4 centered on TOI-1859, which excluded most of the flux from the nearest Gaia DR3 neighbor 10.″3 south.

2. We observed an ingress on UT 2021 May 26 in Pan-STARRS z-short band using the Las Cumbres Observatory Global Telescope (LCOGT; Brown et al. 2013) 1.0 m network node at McDonald Observatory on Mount Fowlkes in Texas, USA. A transit-like ingress with a depth of ∼5000 ppm was detected using a circular photometric aperture with radius 5.″8 centered on TOI-1859, which excluded flux from the nearest Gaia DR3 neighbor 10.″3 south.

2.3. High-resolution Imaging

High-resolution (HR) imaging was performed to search for close companions of TOI-1859. On UT 2020 June 7, the `Alopeke speckle instrument (Scott et al. 2021) on the 8 m Gemini-North telescope located on Hawaii's Maunakea took simultaneous speckle imaging in 832 and 562 nm bands. The 5σ contrast curves were achieved. No companion was detected down to a contrast of 6.36 mag at 0.″5 angular separation in the 832 nm band, and a contrast of 4.31 mag at 0.″5 separation in the 562 nm band, shown in Figure 2. The angular separation of 0.″5 corresponds to a physical distance of 112 au.

2.4. Long-term Spectroscopic Observation

Three spectroscopic observations were taken by Tillinghast Reflector Echelle Spectrograph (TRES) at Whipple Observatory on Mount Hopkins in Arizona, USA. The TRES spectrograph has a wavelength coverage from 385 to 906 nm and a resolving power of $R \approx 44{,}000$ (Fűrész 2008). Radial velocities (RVs) were measured using a cross-correlation analysis against a template spectrum generated from a median combination of all TRES observed spectra (Quinn et al. 2014).

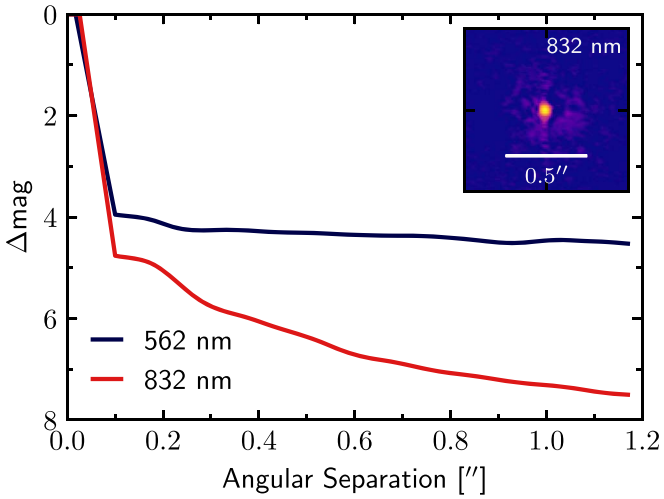

Figure 2. Speckle imaging of TOI-1859 taken by the Gemini-North `Alopeke. Angular separations from 0.″1 to 1″ correspond to physical distances from 22.4 to 224 au. Companions are ruled out to a contrast of 6.36 mag at 0.″5 separation (or a physical distance of 112 au) in the 832 nm band (red curve and the inset image) and a contrast of 4.31 mag at 0.″5 separation in the 562 nm band (blue curve).

Three TRES observations were taken on UT 2020 July 26, UT 2020 September 3, and UT 2022 August 29. We used the highest signal-to-noise spectra taken on UT 2022 August 29 in this study. The Stellar Parameter Classification code (SPC; Buchhave et al. 2012, 2014) was applied to extracted TRES spectra (Buchhave et al. 2010), and derived stellar parameters are used as priors for the stellar spectral energy distribution (SED) joint isochrone modeling in Section 3. The SPC derives an effective temperature of $T_{\rm eff} = 6318 \pm 100$ K, surface gravity $\log g = 4.3 \pm 0.1$ cgs, and bulk metallicity [m/H] = +0.11 ± 0.08 dex. The projected rotational

broadening width $v_{\rm broadening} = 13.1 \pm 0.5$ km s^{-1}, which is introduced by the rotation and macroturbulence of the host star.

Another 23 spectroscopic observations were taken by the Automated Planet Finder (APF) at Lick Observatory on Mount Hamilton in California, USA. The APF spectrograph has a wavelength coverage from 374 to 970 nm with a maximum resolving power $R \approx 150{,}000$ (Radovan et al. 2014; Vogt et al. 2014). The 23 APF observations span over 270 days and present an RV rms of 59 m s^{-1}. The scatter in the APF RVs is mainly contributed by the large $v \sin i_\star$ of the host star (i.e., $v \sin i_\star \sim 13$ km s^{-1}). Also, with $V > 10$ mag, it is beyond the limit of APF to yield reliable RVs.

2.5. Transit Spectroscopy Observation

The transit spectroscopy observation of TOI-1859b was taken by the NEID spectrograph (Halverson et al. 2016; Schwab et al. 2016) on the WIYN 3.5 m telescope at the Kitt Peak National Observatory in Arizona, USA. The NEID spectrograph is a highly stabilized (Stefànsson et al. 2016; Robertson et al. 2019), fiber-fed (Kanodia et al. 2018) spectrograph with a resolving power of $R \approx 110{,}000$ in HR mode and a wavelength coverage from 380 to 930 nm. The NEID observations were conducted on UT 2022 June 11 from 03:30 to 11:30 for a duration of 8 hr. We obtained 23 spectra, each with a 20 minute exposure, in HR mode.

The spectra were extracted, and RVs were reduced by the NEID standard data reduction pipeline `NEID-DRP v1.1.4`.[39] The `DRP` reduces the RVs using the cross correlation of the observed spectra with stellar templates. The barycentric corrected RVs for re-weighted orders (`CCFRVMOD`) were used for the analysis. We separately reduce the RVs using a modified version of the SpEctrum Radial Velocity AnaLyzer (`SERVAL`) pipeline Zechmeister et al. (2018), which reconstructs the stellar template from observations, optimized for NEID spectra. The NEID customization of the `SERVAL` pipeline is discussed in Stefànsson et al. (2022) Section 3.1.

The median RV uncertainty from the `DRP` pipeline was found to be 10.6 m s^{-1}, while the median RV uncertainty from the `SERVAL` pipeline was 6.0 m s^{-1}. The RV uncertainty could be overestimated by the `DRP` pipeline because of some error in the cross-correlation function (CCF) RV calculation, which could have been further exacerbated by the star's high $v \sin i_\star$. Additionally, the `SERVAL` pipeline used more echelle orders than the CCF line mask used in the `DRP`, which could slightly improve the RV uncertainty. Further investigation is needed to fully understand the factors contributing to the difference in RV uncertainties between the two pipelines.

We also derive line-broadening profiles for each observation to measure the Doppler transit shadow of the planet as a function of velocity and phase. The line profile from each spectrum is derived via a least-squares deconvolution (Donati et al. 1997) between the NEID spectra and an ATLAS9 synthetic nonrotating spectral template that best fits the host star stellar parameters (Castelli & Kurucz 2004). See Section 2.6 in Dong et al. (2022) for more details.

[39] https://neid.ipac.caltech.edu/docs/NEID-DRP

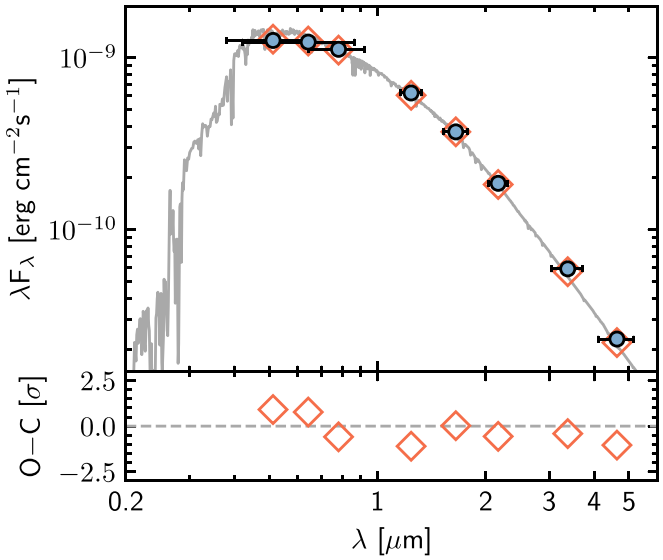

Figure 3. The SED analysis of TOI-1859. Each blue point corresponds to a photometric filter, and the x-axis error bar corresponds to the passband of the filter. The best-fitted SED model is shown in gray. The orange diamond shows the combined synthetic flux over each passband. The SED residuals normalized by the photometric uncertainties are shown in the lower panel.

3. Stellar and Planetary Properties

3.1. Stellar Modeling

The SED of the star is modeled with the `astroARIADNE` package (Vines & Jenkins 2022). Our SED analysis of TOI-1859 uses magnitudes from eight filters including 2MASS J, H, K, Gaia G, Rp, Bp, and WISE W1, W2. We include an additional error scaling factor for the SED model as recommended in `EXOFASTv2` (Eastman et al. 2013, 2019). The error scaling factor usually leads to greater but more realistic stellar radius uncertainties. The PHOENIXv2 models (Husser et al. 2013) and MIST isochrones (Dotter 2016) are applied to the SED and isochrone fits. The SED and the best-fitted model of TOI-1859 are shown in Figure 3. For stellar parameter priors, we adopt $T_{\rm eff}$ and [Fe/H] derived from the TRES spectra. The inferred stellar parameters are $M_\star = 1.287 \pm 0.061\, M_\odot$, $\log_{10}{\rm Age} = 9.15^{+0.27}_{-0.68}$ (yr), [Fe/H] $= 0.12^{+0.054}_{-0.056}$, $R_\star = 1.36^{+0.10}_{-0.12}\, R_\odot$, $T_{\rm eff} = 6341^{+68}_{-70}$ K, and $A_V = 0.18^{+0.27}_{-0.13}$. Consequently, we derive $\rho_\star = 0.73^{+0.21}_{-0.15}$ g cm^{-3} and $\log g = 4.285^{+0.069}_{-0.067}$. These stellar parameters are summarized in Table 1.

For stellar inclination inference, we looked for periodicities in TESS light curves using the periodogram and ACF methods but detected no clear and consistent rotational modulation signal. Any period in the range from 2 to 10 days must have a corresponding amplitude smaller than about 0.05%.

3.2. Transit Modeling

In the transit model, we fit the nine full transits and one partial transit of TOI-1859b detected in TESS SPOC light curves. We model the mid-transit time $T_{0..9}$ for each transit to allow transit-timing variation analysis. TESS light curves are modeled with the `exoplanet` package (Foreman-Mackey et al. 2021). We adopt a quadratic limb-darkening model and add a Matern 3/2 Gaussian process (GP) kernel to the transit model. To reduce computing complexity, TESS light curves are trimmed to roughly 3 times the transit duration before and after

Table 1
Median Values and 68% Highest Density Intervals (HDIs) for the Stellar and Planetary Parameters of the TOI-1859 (TIC-229742722) System

Parameter	Units	Values			
Stellar Properties					
α_{J2016}	Gaia DR3 RA (HH:MM:SS.ss)	18:39:19.62			
δ_{J2016}	Gaia DR3 Dec (DD:MM:SS.ss)	+69:31:22.34			
ϖ	Gaia DR3 parallax (mas)	4.4745 ± 0.0123			
G	Gaia DR3 G magnitude	10.2883 ± 0.0044			
$G_{\rm BP}$	Gaia DR3 $G_{\rm BP}$ magnitude	10.5379 ± 0.0028			
$G_{\rm RP}$	Gaia DR3 $G_{\rm RP}$ magnitude	9.8867 ± 0.0038			
$M_\star$	Stellar mass ($M_\odot$)	1.287 ± 0.061			
$R_\star$	Stellar radius ($R_\odot$)	$1.36^{+0.10}_{-0.12}$			
$\rho_\star$	Stellar density (cgs)	$0.73^{+0.21}_{-0.15}$			
$\log g$	Stellar surface gravity (cgs)	$4.285^{+0.069}_{-0.067}$			
$T_{\rm eff}$	Stellar effective temperature (K)	6341^{+68}_{-70}			
[m/H]	Stellar bulk metallicity (dex)	$0.120^{+0.054}_{-0.056}$			
$\log_{10}$ Age	Age (yr)	$9.15^{+0.27}_{-0.68}$			
$v \sin i_\star$	TRES projected line broadening (km s^{-1})	13.1 ± 0.5			
Stellar/Planetary Properties from transit+RM-effect models					
P	Period (days)	63.48347 ± 0.00010			
T_C	Mid-transit time (BJD−2457000 days)	$1{,}662.6558 \pm 0.0014$			
		Transit-only	With NEID-DRP	With SERVAL	With DT
$\rho_\star$	Fitted stellar density (cgs)	$0.71^{+0.17}_{-0.18}$	$0.72^{+0.19}_{-0.17}$	$0.72^{+0.17}_{-0.18}$	$0.73^{+0.20}_{-0.16}$
$a/R_\star$	Planet–star separation	$53.4^{+4.8}_{-4.0}$	$53.5^{+5.1}_{-4.0}$	$53.5^{+4.8}_{-4.1}$	$53.7^{+4.7}_{-4.0}$
a	Semimajor axis (au)	$0.335^{+0.041}_{-0.040}$	$0.336^{+0.041}_{-0.038}$	$0.336^{+0.040}_{-0.041}$	$0.337^{+0.044}_{-0.036}$
b	Impact parameter	$0.48^{+0.13}_{-0.09}$	$0.51^{+0.08}_{-0.05}$	$0.51^{+0.07}_{-0.06}$	$0.61^{+0.03}_{-0.03}$
i	Orbital inclination (deg)	$88.83^{+0.46}_{-0.58}$	$88.71^{+0.44}_{-0.31}$	$88.70^{+0.43}_{-0.31}$	$88.64^{+0.38}_{-0.28}$
$R_p/R_\star$	Planet–star radius ratio	$0.0651^{+0.0010}_{-0.0008}$	$0.0654^{+0.0007}_{-0.0005}$	$0.0654^{+0.0006}_{-0.0006}$	$0.0660^{+0.0004}_{-0.0005}$
R_p	Planet radius ($R_{\rm Jup}$)	$0.86^{+0.08}_{-0.06}$	$0.87^{+0.07}_{-0.06}$	$0.86^{+0.07}_{-0.07}$	$0.87^{+0.07}_{-0.07}$
e	Eccentricity	$0.66^{+0.13}_{-0.16}$	$0.64^{+0.12}_{-0.17}$	$0.64^{+0.11}_{-0.17}$	$0.57^{+0.12}_{-0.16}$
ω	Argument of periapse (deg)	$77.2^{+78.1}_{-56.8}$	$78.2^{+82.6}_{-54.3}$	$80.5^{+90.3}_{-45.8}$	$79.9^{+83.2}_{-48.2}$
λ	Projected stellar obliquity (deg)	…	$46.7^{+7.4}_{-7.6}$	$47.5^{+5.7}_{-6.0}$	$38.9^{+2.8}_{-2.7}$
$v \sin i_\star$	Fitted projected line broadening (km s^{-1})	…	$13.22^{+0.47}_{-0.49}$	$13.27^{+0.51}_{-0.42}$	$12.49^{+0.33}_{-0.33}$
$v_{\rm macro}$	Macroturbulence of the host star (km s^{-1})	…	…	…	$2.87^{+0.14}_{-0.13}$
$\sigma_{\rm RV}$	Radial velocity jitter (m s^{-1})	…	$1.52^{+0.96}_{-1.50}$	$1.51^{+0.95}_{-1.50}$	…

Note. Gaia magnitudes and spectral line-broadening parameter are obtained from the Gaia Data Release 3 (Gaia Collaboration et al. 2023). Planetary parameters inferred from the Doppler tomography signal are used for discussion.

the transit. Even though we model each mid-transit time independently, an orbital period is still required to build the Keplerian orbit of the planet and is fixed at 63.4832 days. The period (P) and a reference mid-transit time (T_C) are later derived from a linear fit using the posteriors of mid-transit times. Here we list free parameters in our transit model: $\{\rho_\star, b, R_{\rm p}/R_\star, T_{0..9}, e, \omega, u_0, u_1\}$ and GP hyperparameters $\{{\rm GP}_{s,0..9}, {\rm GP}_{\sigma,0..9}, {\rm GP}_{\rho,0..9}\}$. The planet–star radius ratio $R_{\rm p}/R_\star$ and GP kernel hyperparameters ${\rm GP}_s$, ${\rm GP}_\sigma$, and ${\rm GP}_\rho$ are reparameterized to their logarithm forms, eccentricity and argument of periapse $\{e, \omega\}$ to the unit disk distribution as $\{\sqrt{e}\cos\omega, \sqrt{e}\sin\omega\}$, and limb-darkening coefficients $\{u_0, u_1\}$ to the ones described in Kipping (2013). We take the stellar density $\rho_\star$ prior from the SED fit and use uniform priors for the remaining parameters. The posteriors are sampled using the gradient-based MCMC algorithm, the No-U-Turn Sampler, built in the PyMC package. A summary of the medians and 94% highest density intervals (HDIs) of the fitted parameters are summarized in Table 1 in the "Transit-only" column.

The transit-timing variation (TTV) is derived from the deviations of the mid-transit times from a linear trend. TOI-1859b's TTV has an rms of 3 minutes, compared to the averaged mid-transit time uncertainty of 2 minutes. The TTV signal does not present an obvious sinusoidal pattern, and it is unclear if the variation is introduced by a nearby companion.

3.3. Rossiter–McLaughlin Effect Modeling

We next model the NEID RM-effect measurement jointly with the TESS transits. In addition to the previous transit model, we now add another component to fit the RV anomalies due to the RM effect. We adopt the expression for the RM-effect RV anomaly in Hirano et al. (2011) Equations (16)–(18), which assumes a Gaussian line profile convolving with a rotational-macroturbulent broadening kernel. To incorporate the integrals in Hirano et al. (2011)'s description to the gradient-based sampling code PyMC, we evaluate the integrals numerically using a trapezoidal approximation. New added parameters include the sky-projected stellar obliquity λ, the sky-projected rotational broadening of the stellar rotation $v \sin i_\star$, the RV jitter $\sigma_{\rm RV}$, and the quadratic limb-darkening coefficients for the NEID filter. We use a uniform prior on λ, a Gaussian prior on $v \sin i_\star$ derived from the TRES SPC, and a log uniform prior on $\sigma_{\rm RV}$. The model also has three more free parameters described in the Hirano et al. (2011) model: the Gaussian dispersion of spectral lines β, the Lorentzian dispersion of spectral lines γ, and the macroturbulence

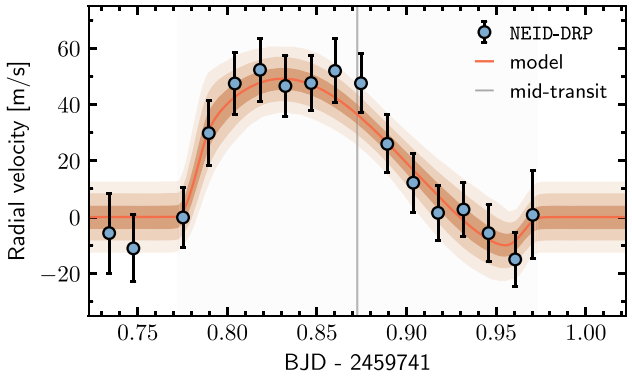

(a) In-transit radial velocities reduced by the NEID-DRP v1.1.4 pipeline which infer $\lambda = 46.7^{+7.4}_{-7.6}{}^{\circ}$.

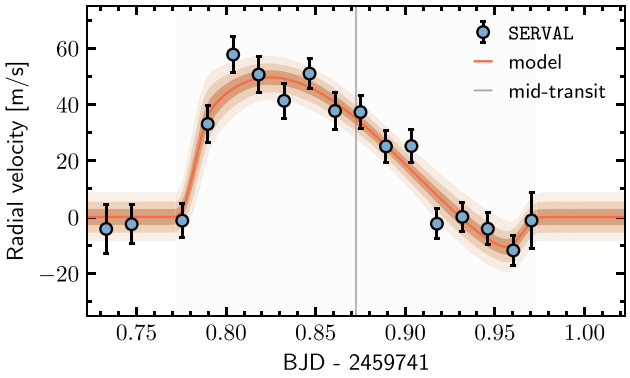

(b) In-transit radial velocities reduced by the SERVAL pipeline which infer $\lambda = 47.5^{+5.7}_{-6.0}{}^{\circ}$.

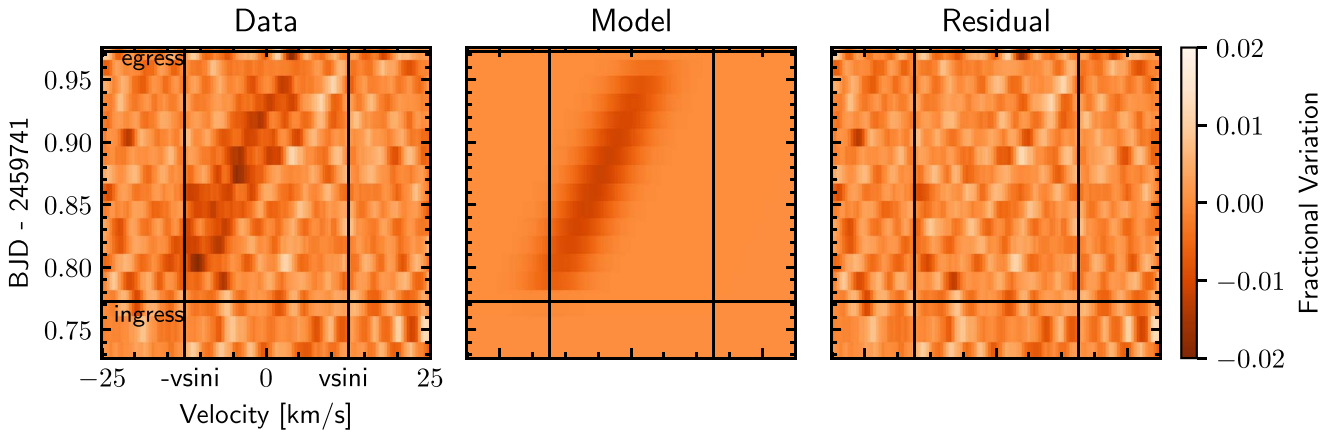

(c) Doppler Tomography signal which infers $\lambda = 38.9^{+2.8}_{-2.7}{}^{\circ}$.

Figure 4. NEID spectra are reduced by three different data reduction techniques. Inferred projected stellar obliquities are consistent. (a) and (b) In-transit RV measurements of the TOI-1859 system using the NEID spectra. The blue dots and black bars are NEID RVs and their corresponding uncertainties. Using the RM effect, the projected stellar obliquity is constrained. (c) The Doppler Tomography signal of the TOI-1859 system during TOI-1859b's transit. The left, middle, and right panels are data extracted from the NEID spectra, best-fit model, and the residual of the data after subtracting the best-fit model. The color scale presents the flux variation of the velocity channel.

dispersion ζ. We set uniform priors on these parameters using the typical ranges listed in Hirano et al. (2011) Table 1.

For the Doppler Tomography signal, we model the velocity profile of the planetary shadow at each exposure, and from the mean velocity of the planet, we infer the location of the planet on the stellar disk relative to the stellar rotation axis. For the planetary shadow, we use a Gaussian profile with a width of $\sigma = \sqrt{v_0^2 + v_{\rm macro}^2}$, where v_0 is set by the resolution of the spectrograph and $v_{\rm macro}$ is the macroturbulence velocity of the star. A log uniform prior is used on $v_{\rm macro}$, broadly distributed from 0.1 to 50 $\rm km\,s^{-1}$, to avoid an underestimation on v_0.

Again, we use the PyMC package for the posterior sampling and report the medians and 94% HDI for the fitted parameters. In Figure 4, we present the RM-effect fit results. The inferred sky-projected stellar obliquity λ is $38.9^{+2.8}_{-2.7}{}^{\circ}$ inferred from the Doppler tomography (DT) signal, $47.5^{+5.7}_{-6.0}{}^{\circ}$ from the SERVAL RVs, and $46.7^{+7.4}_{-7.6}{}^{\circ}$ from the NEID-DRP RVs. Planetary parameters inferred from the joint fit are listed in Table 1. Inferred parameters from the NEID-DRP RVs and the SERVAL RVs are completely consistent within the uncertainty. The λ and $v \sin i_\star$ inferred from the RV models are also consistent with the ones inferred from the DT model.

4. Discussion

TOI-1859b is a 64 day Jupiter-sized planet discovered during the TESS mission. We confirmed the planetary nature of TOI-1859b and measured the obliquity of TOI-1859 using the NEID spectrograph. Notably, TOI-1859b is the second-longest-period planet with an RM-effect measurement after HD 80606b (see Figure 5). We jointly model the planet's transit light curves and the RM-effect signals to constrain its orbital properties. We find a semimajor axis of $0.337^{+0.044}_{-0.036}$ au, an eccentricity of $0.57^{+0.12}_{-0.16}$, and a sky-projected stellar obliquity of $38.9^{+2.8}_{-2.7}{}^{\circ}$. Due to the lack of precise long-term RV data, the eccentricity of TOI-1859b is constrained only by the transit light curves. From the sky-projected stellar obliquity, it is possible to further infer the *true* stellar obliquity of TOI-1859 although the inference will be compromised by the unknown stellar inclination. If we assume an isotropic stellar inclination (i.e., $\cos i_\star$ is uniformly distributed), the inferred stellar obliquity is $\psi = 41.5^{+4.9}_{-10.0}{}^{\circ}$. The mode and 68% HDI are reported since the probability density distribution of ψ is skewed. TOI-1859b is unlikely to have strong tidal interactions with its host star given its large semimajor axis and moderate eccentricity.

The speckle imaging rules out nearby companions at the instrumental detection limit. TOI-1859 has a Renormalized

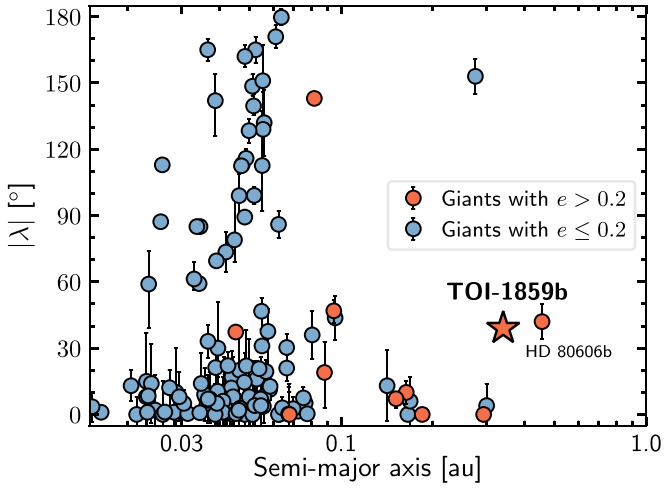

Figure 5. Sky-projected stellar obliquity vs. the semimajor axis of all measured giant planets colored by their eccentricities. Eccentric orbits with median $e > 0.2$ are colored in orange, and circular orbits with $e \leqslant 0.2$ are colored in blue. Literature data are extracted from Table A1 in Albrecht et al. (2022).

Unit Weight Error number of 1.11 but an excess of astrometric noise. We performed a crossmatch with the Gaia DR3 binaries catalog (El-Badry et al. 2021) and identified a likely bound companion at a sky-plane separation of 2360 au ($\approx 10''$) with $G \approx 20$ mag, with a chance alignment probability of $\approx 9 \times 10^{-4}$ (primary source: Gaia DR3 2259354802894412928; secondary source: Gaia DR3 2259354802893022208). The value of $G_{\rm BP} - G_{\rm RP}$ of the companion is significantly impacted by the contamination of the primary, but from the absolute G magnitude, the companion star is likely a late-type M dwarf. However, the companion separation is sufficiently large such that it is unlikely to overcome GR precession to induce stellar Kozai oscillation on TOI-1859b when using the criteria in Equation (4) in Dong et al. (2014).

The excitation of TOI-1859b's high eccentricity is likely a result of dynamic interactions between multiple planets in the system, such as planet–planet scattering (Nagasawa & Ida 2011; Beaugé & Nesvorný 2012) and planetary Kozai (Petrovich & Tremaine 2016). If TOI-1859b's eccentricity and inclination are indeed excited by the planetary Kozai, we may expect a nearby planetary companion still coupled to TOI-1859b to explain its current relatively low eccentricity. The obliquity of TOI-1859 could also be consistent with the prediction of the planet–disk resonance crossing due to the protoplanetary disk dissipation in a warm Jupiter system (Petrovich et al. 2020; J. Zanazzi & E. Chiang 2023, in preparation). If so, it requires a massive outer companion in the TOI-1859 system to allow sufficient angular momentum exchange with TOI-1859b. In any of these scenarios, it is worthwhile to conduct long-term RV follow-up to detect any other planetary/brown dwarf candidates and constrain their mass and orbit.

TOI-1859 is a massive, metal-rich star with a stellar mass of 1.287 ± 0.061 and a bulk metallicity [m/H] of $0.120^{+0.054}_{-0.056}$. TOI-1859b's eccentric and misaligned orbit, likely a result of planet–planet interactions, is consistent with the host star metallicity–eccentricity trend found in Dawson & Murray-Clay (2013). It is also consistent with the "eccentric migration" framework proposed by Wu et al. (2023): multiple gas giants are more likely to form around metal-rich stars and can dynamically interact to excite their orbital eccentricities and mutual inclinations. Furthermore, TOI-1859 is a hot star with an effective temperature of 6341^{+68}_{-70} K. It is yet unclear if the temperature–stellar obliquity trend found in hot Jupiter systems (Schlaufman 2010; Winn et al. 2010) is also true in warm Jupiter systems. At least for TOI-1859b, it is consistent with the trend that misaligned planets are often found around hot stars. Detecting and characterizing more warm Jupiter systems like TOI-1859b around both cool and hot stars will fill out the parameter space and reveal any possible trends between host star effective temperature and stellar obliquity in warm Jupiter systems.

Acknowledgments

We would like to express our sincere gratitude to Fei Dai, Dan Foreman-Mackey, and Rodrigo Luger for their helpful discussions on data modeling. We would like to thank Kareem El-Badry for interpretations of the Gaia data.

Data presented were obtained by the NEID spectrograph built by Penn State University and operated at the WIYN Observatory by NOIRLab, under the NN-EXPLORE partnership of the National Aeronautics and Space Administration and the National Science Foundation. These results are based on observations obtained with NEID on the WIYN 3.5 m Telescope at Kitt Peak National Observatory (PI: Songhu Wang; 2022A-763446 IU TAC). WIYN is a joint facility of the University of Wisconsin-Madison, Indiana University, NSF's NOIRLab, the Pennsylvania State University, Purdue University, University of California, Irvine, and the University of Missouri. The authors are honored to be permitted to conduct astronomical research on Iolkam Du'ag (Kitt Peak), a mountain with particular significance to the Tohono O'odham.

The Pennsylvania State University campuses are located on the original homelands of the Erie, Haudenosaunee (Seneca, Cayuga, Onondaga, Oneida, Mohawk, and Tuscarora), Lenape (Delaware Nation, Delaware Tribe, Stockbridge-Munsee), Shawnee (Absentee, Eastern, and Oklahoma), Susquehannock, and Wahzhazhe (Osage) Nations. As a land grant institution, we acknowledge and honor the traditional caretakers of these lands and strive to understand and model their responsible stewardship. We also acknowledge the longer history of these lands and our place in that history. The Center for Exoplanets and Habitable Worlds and the Penn State Extraterrestrial Intelligence Center are supported by the Pennsylvania State University and the Eberly College of Science.

Some of the data presented in this paper were obtained from the Mikulski Archive for Space Telescopes (MAST) at the Space Telescope Science Institute. The specific observations analyzed can be accessed via doi:10.17909/t9-nmc8-f686. This work includes data collected by the TESS mission, which are publicly available from MAST. Funding for the TESS mission is provided by the NASA Science Mission directorate. We acknowledge the use of public TESS data from pipelines at the TESS Science Office and at the TESS Science Processing Operations Center. Resources supporting this work were provided by the NASA High-End Computing (HEC) Program through the NASA Advanced Supercomputing (NAS) Division at Ames Research Center for the production of the SPOC data products. This research has made use of the Exoplanet Follow-up Observation Program website, which is operated by the California Institute of Technology, under contract with the National Aeronautics and Space Administration under the

Exoplanet Exploration Program. Some of the data presented in this paper were obtained from MAST. Support for MAST for non-HST data is provided by the NASA Office of Space Science via grant NNX09AF08G and by other grants and contracts. This work has made use of data from the European Space Agency (ESA) mission Gaia (https://cosmos.esa.int/gaia), processed by the Gaia Data Processing and Analysis Consortium (DPAC; https://cosmos.esa.int/web/gaia/dpac/consortium). Funding for the DPAC has been provided by national institutions, in particular the institutions participating in the Gaia Multilateral Agreement. This research has made use of the NASA Exoplanet Archive, which is operated by the California Institute of Technology, under contract with the National Aeronautics and Space Administration under the Exoplanet Exploration Program.

Some of the observations in the paper made use of the High-Resolution Imaging instrument(s) `Alopeke. `Alopeke was funded by the NASA Exoplanet Exploration Program and built at the NASA Ames Research Center by Steve B. Howell, Nic Scott, Elliott P. Horch, and Emmett Quigley. `Alopeke was mounted on the Gemini-North telescope of the international Gemini Observatory, a program of NSF's NOIRLab, which is managed by the Association of Universities for Research in Astronomy (AURA) under a cooperative agreement with the National Science Foundation on behalf of the Gemini Observatory partnership: the National Science Foundation (United States), National Research Council (Canada), Agencia Nacional de Investigación y Desarrollo (Chile), Ministerio de Ciencia, Tecnología e Innovación (Argentina), Ministério da Ciência, Tecnologia, Inovações e Comunicações (Brazil), and Korea Astronomy and Space Science Institute (Republic of Korea).

This work makes use of observations from the LCOGT network. Part of the LCOGT telescope time was granted by NOIRLab through the Mid-Scale Innovations Program (MSIP). MSIP is funded by NSF.

J.A.A.-M. is funded by the International Macquarie University Research Excellence Scholarship ("iMQRES"). G. S. acknowledges support provided by NASA through the NASA Hubble Fellowship grant HST-HF2-51519.001-A awarded by the Space Telescope Science Institute, which is operated by the Association of Universities for Research in Astronomy, Inc., for NASA, under contract NAS5-26555. R.I. D. gratefully acknowledges support from the Carnegie Institution for Science Tuve Visiting Scientists program. This research was carried out, in part, at the Jet Propulsion Laboratory, California Institute of Technology, under a contract with the National Aeronautics and Space Administration (80NM0018D0004). K.A.C., S.N.Q., and D.W.L. acknowledge support from the TESS mission via subaward s3449 from MIT. D.D. acknowledges support from the NASA Exoplanet Research Program grant 18-2XRP18_2-0136. M.R., P.D., and S.W. thank the Heising-Simons Foundation for their generous support. D.R. was supported by NASA under award number NNA16BD14C for NASA Academic Mission Services.

This research made use of `exoplanet` (Foreman-Mackey et al. 2019, 2021) and its dependencies (Astropy Collaboration et al. 2013, 2018; Kipping 2013; Salvatier et al. 2016; Theano Development Team 2016; Foreman-Mackey et al. 2017, 2019; Foreman-Mackey 2018; Luger et al. 2019; Agol et al. 2020).

Facilities: TESS, WIYN (NEID), Gemini-North (`Alopeke), Gaia, LCOGT, TRES, APF, Exoplanet Archive.

Software: `ArviZ` (Kumar et al. 2019), `astroARIADNE`, `AstroImageJ` (Collins et al. 2017), `astropy` (Astropy Collaboration et al. 2013, 2018), `celerite2` (Foreman-Mackey et al. 2017; Foreman-Mackey 2018), `exoplanet` (Foreman-Mackey et al. 2019, 2021), `Jupyter` (Kluyver et al. 2016), `Matplotlib` (Hunter 2007; Droettboom et al. 2016), `NumPy` (van der Walt et al. 2011; Harris et al. 2020), `pandas` (McKinney 2010; pandas development team 2020), `PyMC3` (Salvatier et al. 2016), `SciPy` (Virtanen et al. 2020), `starry` (Luger et al. 2019), `Tapir` (Jensen 2013).

Appendix
Supplementary Figures

In this section, we include supplementary figures for the stellar and planetary analysis discussed in Section 3. In Figure 6, we show each individual TESS transit light curves of TOI-1859b, along with the fitted transit model and residuals. In Figure 7, we present the corner plot of the posteriors from the transit joint RM-effect fit discussed in Section 3.3. Posteriors from the `NEID-DRP` RVs, `SERVAL` RVs, and Doppler tomography data are shown.

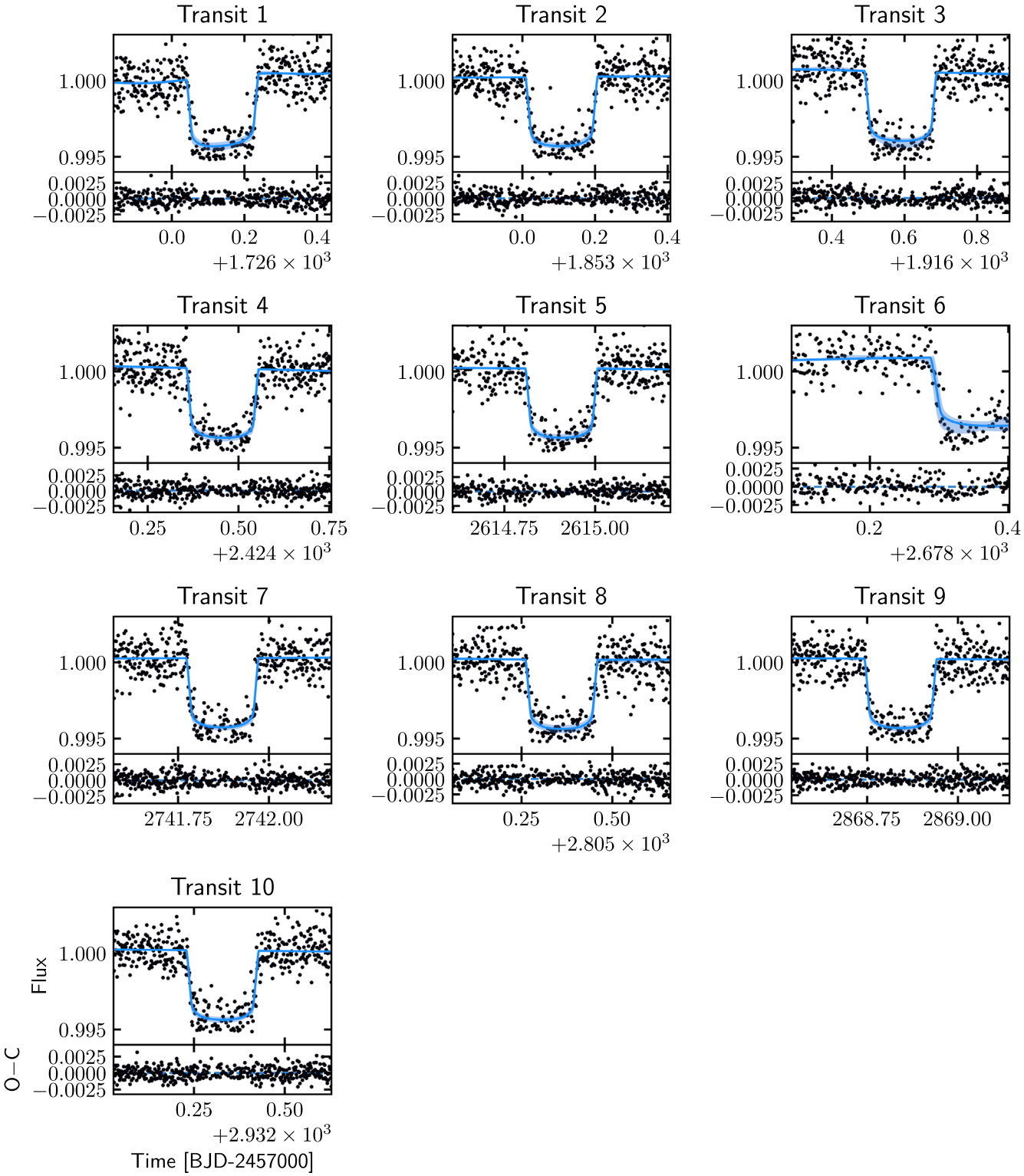

Figure 6. Individual TESS transits of TOI-1859b. The medians and 3σ uncertainties of the fitted transit model are plotted in blue lines and light blue contours, respectively.

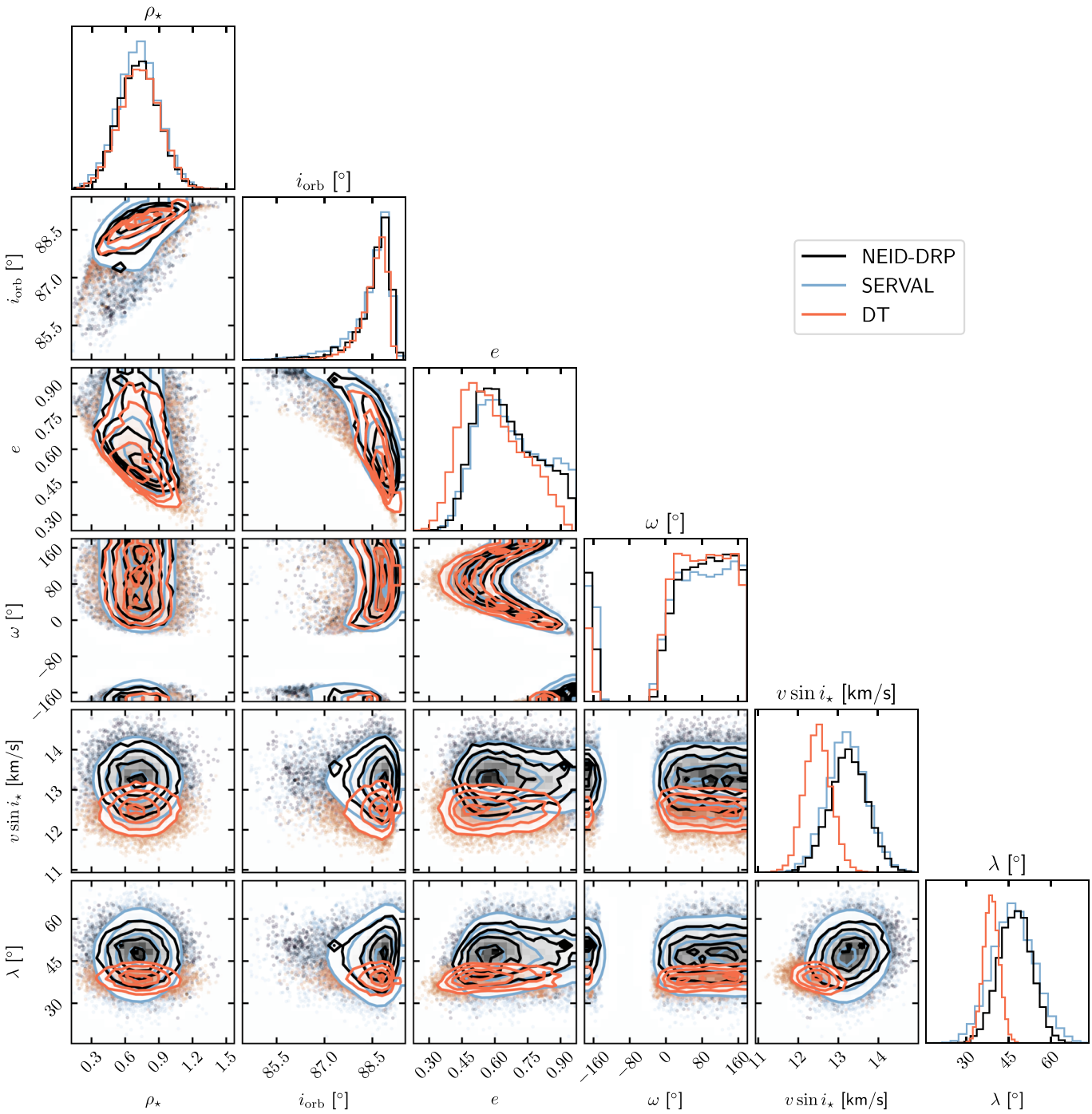

Figure 7. Corner plots of the posteriors of the inferred orbital parameters from the NEID-DRP RVs in black, SERVAL RVs in blue, and Doppler Tomography in orange.

ORCID iDs

Jiayin Dong https://orcid.org/0000-0002-3610-6953
Songhu Wang https://orcid.org/0000-0002-7846-6981
Malena Rice https://orcid.org/0000-0002-7670-670X
George Zhou https://orcid.org/0000-0002-4891-3517
Chelsea X. Huang https://orcid.org/0000-0003-0918-7484
Rebekah I. Dawson https://orcid.org/0000-0001-9677-1296
Gudmundur K. Stefánsson https://orcid.org/0000-0001-7409-5688
Samuel Halverson https://orcid.org/0000-0003-1312-9391
Shubham Kanodia https://orcid.org/0000-0001-8401-4300
Suvrath Mahadevan https://orcid.org/0000-0001-9596-7983
Michael W. McElwain https://orcid.org/0000-0003-0241-8956
Jaime A. Alvarado-Montes https://orcid.org/0000-0003-0353-9741
Joe P. Ninan https://orcid.org/0000-0001-8720-5612
Paul Robertson https://orcid.org/0000-0003-0149-9678
Arpita Roy https://orcid.org/0000-0001-8127-5775
Christian Schwab https://orcid.org/0000-0002-4046-987X
Sarah E. Logsdon https://orcid.org/0000-0002-9632-9382
Ryan C. Terrien https://orcid.org/0000-0002-4788-8858
Karen A. Collins https://orcid.org/0000-0001-6588-9574
Ramotholo Sefako https://orcid.org/0000-0003-3904-6754
David W. Latham https://orcid.org/0000-0001-9911-7388
Allyson Bieryla https://orcid.org/0000-0001-6637-5401
Paul A. Dalba https://orcid.org/0000-0002-4297-5506
Diana Dragomir https://orcid.org/0000-0003-2313-467X
Steven Villanueva, Jr. https://orcid.org/0000-0001-6213-8804
Steve B. Howell https://orcid.org/0000-0002-2532-2853
George R. Ricker https://orcid.org/0000-0003-2058-6662
S. Seager https://orcid.org/0000-0002-6892-6948
Joshua N. Winn https://orcid.org/0000-0002-4265-047X
Jon M. Jenkins https://orcid.org/0000-0002-4715-9460
Avi Shporer https://orcid.org/0000-0002-1836-3120
David Rapetti https://orcid.org/0000-0003-2196-6675

References

Agol, E., Luger, R., & Foreman-Mackey, D. 2020, AJ, 159, 123
Albrecht, S., Winn, J. N., Johnson, J. A., et al. 2012, ApJ, 757, 18
Albrecht, S. H., Dawson, R. I., & Winn, J. N. 2022, PASP, 134, 082001
Anderson, K. R., Storch, N. I., & Lai, D. 2016, MNRAS, 456, 3671
Astropy Collaboration, Price-Whelan, A. M., Sipőcz, B. M., et al. 2018, AJ, 156, 123
Astropy Collaboration, Robitaille, T. P., Tollerud, E. J., et al. 2013, A&A, 558, A33
Beaugé, C., & Nesvorný, D. 2012, ApJ, 751, 119
Brown, T. M., Baliber, N., Bianco, F. B., et al. 2013, PASP, 125, 1031
Buchhave, L. A., Bizzarro, M., Latham, D. W., et al. 2014, Natur, 509, 593
Buchhave, L. A., Bakos, G. Á., Hartman, J. D., et al. 2010, ApJ, 720, 1118
Buchhave, L. A., Latham, D. W., Johansen, A., et al. 2012, Natur, 486, 375
Castelli, F., & Kurucz, R. L. 2004, A&A, 419, 725
Chatterjee, S., Ford, E. B., Matsumura, S., & Rasio, F. A. 2008, ApJ, 686, 580
Collins, K. 2019, AAS Meeting Abstracts, 233, 140.05
Collins, K. A., Kielkopf, J. F., Stassun, K. G., & Hessman, F. V. 2017, AJ, 153, 77
Dawson, R. I., & Murray-Clay, R. A. 2013, ApJL, 767, L24
Donati, J. F., Semel, M., Carter, B. D., Rees, D. E., & Collier Cameron, A. 1997, MNRAS, 291, 658
Dong, J., Huang, C. X., Dawson, R. I., et al. 2021, ApJS, 255, 6
Dong, J., Huang, C. X., Zhou, G., et al. 2022, ApJL, 926, L7
Dong, S., Katz, B., & Socrates, A. 2014, ApJL, 781, L5
Dotter, A. 2016, ApJS, 222, 8
Droettboom, M., Hunter, J., Caswell, T. A., et al. 2016, Matplotlib: Matplotlib, v1.5.1, Zenodo, doi:10.5281/zenodo.44579
Duffell, P. C., & Chiang, E. 2015, ApJ, 812, 94
Eastman, J., Gaudi, B. S., & Agol, E. 2013, PASP, 125, 83
Eastman, J. D., Rodriguez, J. E., Agol, E., et al. 2019, arXiv:1907.09480
El-Badry, K., Rix, H.-W., & Heintz, T. M. 2021, MNRAS, 506, 2269
Fabrycky, D., & Tremaine, S. 2007, ApJ, 669, 1298
Foreman-Mackey, D. 2018, RNAAS, 2, 31
Foreman-Mackey, D., Agol, E., Ambikasaran, S., & Angus, R. 2017, AJ, 154, 220
Foreman-Mackey, D., Czekala, I., Luger, R., et al. 2019, dfm/exoplanet: exoplanet v0.2.1, Zenodo, doi:10.5281/zenodo.3462740
Foreman-Mackey, D., Luger, R., Agol, E., et al. 2021, JOSS, 6, 3285
Fűrész, G. 2008, PhD thesis, Univ. Szeged, Hungary
Gaia Collaboration, Vallenari, A., Brown, A. G. A., et al. 2023, A&A, 674, A1
Halverson, S., Terrien, R., Mahadevan, S., et al. 2016, Proc. SPIE, 9908, 99086P
Harris, C. R., Millman, K. J., van der Walt, S. J., et al. 2020, Natur, 585, 357
Hirano, T., Suto, Y., Winn, J. N., et al. 2011, ApJ, 742, 69
Huang, C. X., Vanderburg, A., Pál, A., et al. 2020a, RNAAS, 4, 204
Huang, C. X., Vanderburg, A., Pál, A., et al. 2020b, RNAAS, 4, 206
Hunter, J. D. 2007, CSE, 9, 90
Husser, T.-O., von Berg, S. W., Dreizler, S., et al. 2013, A&A, 553, A6
Jenkins, J. M. 2002, ApJ, 575, 493
Jenkins, J. M., Chandrasekaran, H., McCauliff, S. D., et al. 2010, Proc. SPIE, 7740, 77400D
Jenkins, J. M., Tenenbaum, P., Seader, S., et al. 2020, Kepler Data Processing Handbook: Transiting Planet Search, Kepler Science Document KSCI-19081-003, 9
Jenkins, J. M., Twicken, J. D., McCauliff, S., et al. 2016, Proc. SPIE, 9913, 99133E
Jensen, E. 2013, Tapir: A Web Interface for Transit/Eclipse Observability, Astrophysics Source Code Library, ascl:1306.007
Kanodia, S., Mahadevan, S., Ramsey, L. W., et al. 2018, Proc. SPIE, 10702, 107026Q
Kipping, D. M. 2013, MNRAS, 435, 2152
Kluyver, T., Ragan-Kelley, B., Pérez, F., et al. 2016, in Positioning and Power in Academic Publishing: Players, Agents and Agendas, ed. F. Loizides & B. Scmidt (Netherlands: IOS Press), 87
Kozai, Y. 1962, AJ, 67, 591
Kumar, R., Carroll, C., Hartikainen, A., & Martin, O. 2019, JOSS, 4, 1143
Li, J., Tenenbaum, P., Twicken, J. D., et al. 2019, PASP, 131, 024506
Lidov, M. L. 1962, P&SS, 9, 719
Luger, R., Agol, E., Foreman-Mackey, D., et al. 2019, AJ, 157, 64
McLaughlin, D. B. 1924, ApJ, 60, 22
McKinney, W. 2010, in Proc. 9th Python in Science Conf., ed. S. van der Walt & J. Millman (Austin, TX: SciPy), 56
Nagasawa, M., & Ida, S. 2011, ApJ, 742, 72
Nagasawa, M., Ida, S., & Bessho, T. 2008, ApJ, 678, 498
Naoz, S. 2016, ARA&A, 54, 441
Ogilvie, G. I. 2014, ARA&A, 52, 171
pandas development team, T 2020, pandas-dev/pandas: Pandas, v1.4.2, Zenodo, doi:10.5281/zenodo.3509134
Petrovich, C. 2015, ApJ, 799, 27
Petrovich, C., Muñoz, D. J., Kratter, K. M., & Malhotra, R. 2020, ApJL, 902, L5
Petrovich, C., & Tremaine, S. 2016, ApJ, 829, 132
Quinn, S. N., White, R. J., Latham, D. W., et al. 2014, ApJ, 787, 27
Radovan, M. V., Lanclos, K., Holden, B. P., et al. 2014, Proc. SPIE, 9145, 91452B
Rice, M., Wang, S., Gerbig, K., et al. 2023, AJ, 165, 65
Rice, M., Wang, S., Howard, A. W., et al. 2021, AJ, 162, 182
Rice, M., Wang, S., & Laughlin, G. 2022a, ApJL, 926, L17
Rice, M., Wang, S., Wang, X.-Y., et al. 2022b, AJ, 164, 104
Ricker, G. R., Winn, J. N., Vanderspek, R., et al. 2015, JATIS, 1, 014003
Robertson, P., Anderson, T., Stefansson, G., et al. 2019, JATIS, 5, 015003
Rossiter, R. A. 1924, ApJ, 60, 15
Salvatier, J., Wiecki, T. V., & Fonnesbeck, C. 2016, PeerJ Computer Science, 2, e55
Schlaufman, K. C. 2010, ApJ, 719, 602
Schwab, C., Rakich, A., Gong, Q., et al. 2016, Proc. SPIE, 9908, 99087H
Scott, N. J., Howell, S. B., Gnilka, C. L., et al. 2021, FrASS, 8, 138
Smith, J. C., Stumpe, M. C., Van Cleve, J. E., et al. 2012, PASP, 124, 1000
Stefànsson, G., Hearty, F., Robertson, P., et al. 2016, ApJ, 833, 175
Stefànsson, G., Mahadevan, S., Petrovich, C., et al. 2022, ApJ, 931, L15
Stumpe, M. C., Smith, J. C., Catanzarite, J. H., et al. 2014, PASP, 126, 100
Stumpe, M. C., Smith, J. C., Van Cleve, J. E., et al. 2012, PASP, 124, 985
Teyssandier, J., Lai, D., & Vick, M. 2019, MNRAS, 486, 2265
Theano Development Team 2016, arXiv:1605.02688

Twicken, J. D., Catanzarite, J. H., Clarke, B. D., et al. 2018, PASP, 130, 064502
van der Walt, S., Colbert, S. C., & Varoquaux, G. 2011, CSE, 13, 22
Vick, M., Lai, D., & Anderson, K. R. 2019, MNRAS, 484, 5645
Vines, J. I., & Jenkins, J. S. 2022, MNRAS, 513, 2719
Virtanen, P., Gommers, R., Oliphant, T. E., et al. 2020, NatMe, 17, 261
Vogt, S. S., Radovan, M., Kibrick, R., et al. 2014, PASP, 126, 359
von Zeipel, H. 1910, AN, 183, 345
Wang, S., Winn, J. N., Addison, B. C., et al. 2021, AJ, 162, 50
Wang, X.-Y., Rice, M., Wang, S., et al. 2022, ApJL, 926, L8
Winn, J. N., Fabrycky, D., Albrecht, S., & Johnson, J. A. 2010, ApJL, 718, L145
Wu, D.-H., Rice, M., & Wang, S. 2023, AJ, 165, 171
Wu, Y., & Lithwick, Y. 2011, ApJ, 735, 109
Wu, Y., & Murray, N. 2003, ApJ, 589, 605
Zechmeister, M., Reiners, A., Amado, P. J., et al. 2018, A&A, 609, A12